Available online at www.sciencedirect.com
ScienceDirect
Trans. Nonferrous Met. Soc. China 26(2016) 1146−1154
Transactions of Nonferrous Metals Society of China
www.tnmsc.cn

In situ investigation of atmospheric corrosion behavior of PCB-ENIG under adsorbed thin electrolyte layer

Pan YI[1], Kui XIAO[1], Kang-kang DING[1,2], Gang LI[1], Chao-fang DONG[1], Xiao-gang LI[1,3]

1. Corrosion and Protection Center, University of Science and Technology Beijing, Beijing 100083, China;
2. State Key Laboratory for Marine Corrosion and Protection,
Luoyang Ship Material Research Institute, Qingdao 266101, China;
3. Ningbo Institute of Material Technology & Engineering, Chinese Academy of Sciences, Ningbo 315201, China

Received 3 May 2015; accepted 31 October 2015

Abstract: The effects of relative humidity (RH) on a printed circuit board finished with electroless nickel immersion gold (PCB-ENIG) under an adsorbed thin electrolyte layer (ATEL) were investigated in situ via the measurement of cathodic polarization curves, electrochemical impedance spectroscopy, scanning electron microscopy, energy-dispersive X-ray spectroscopy, and X-ray photoelectron spectroscopy to clearly elaborate the corrosion behavior of PCB-ENIG in the atmospheric environment. Results indicated that the cathodic process of PCB-ENIG under ATEL was dominated by the reduction of dissolved oxygen, corrosion products, and H_2O. The cathodic current density of PCB-ENIG increased progressively with increasing RH. Moreover, its cathodic current density in the solution was greater than that under ATEL. This result demonstrated that the diffusion process was not the controlling step during the limiting reduction of cathodic oxygen. When the polarization potentials were located in a more negative region, the cathodic polarization current density gradually decreased under 75% and 85% RH. Notably, the anodic process became the controlling step in the extremely thin liquid film during the remainder of the experiment.

Key words: electronic materials; adsorbed thin electrolyte layer; cathodic polarization curve; electrochemical impedance spectroscopy; relative humidity

1 Introduction

As electronic technology continuously develops, printed circuit boards (PCBs), as electronic components, are moving toward further miniaturization and a highly integrated direction [1]. The trade-off for these technological advances is that electronic devices are becoming increasingly sensitive to moisture and pollutants so that they are more likely to failures because of corrosion [2]. To improve the corrosion resistance capability and weldability of PCBs, various surface coating treatments have been adopted. The electroless nickel immersion gold (ENIG) plating technique has become one of the main surface treatments for PCBs because it provides superior weldability, excellent conductivity, and low contact resistance [3,4].

Electronic components mainly undergo atmospheric corrosion given that 90% of these components are working in the atmospheric environment. Atmospheric corrosion is one of the widespread forms of metallic corrosion. It occurs on a metal surface covered with a thin layer of dilute electrolyte produced by condensation or adsorption. A change in the thickness of the electrolyte layer affects several corrosion-related processes, such as the mass transport of dissolved oxygen, the accumulation of corrosion products, and the hydration of dissolved metal ions [5]. Thus, electrolyte thickness has an important role in the atmospheric corrosion of PCB finished with ENIG (PCB-ENIG). Many investigations on metal or alloy corrosion under a thin electrolyte layer (TEL) have been reported during the past decades [6−8]. ZOU et al [9] studied the corrosion behavior of PCB under wet H_2S environment and found that galvanic corrosion induced by micropores would likely occur in PCB-ENIG. Moreover, the expansion of corrosion products led to the shedding of the surface layer of the protective coating, which might result in the short circuit

Foundation item: Project (51271032) supported by the National Natural Science Foundation of China; Project (2014CB643300) supported by the National Basic Research Program of China; Project supported by the National Environmental Corrosion Platform, China
Corresponding author: Kui XIAO; Tel: +86-10-62333975-522; E-mail: xiaokui@sina.com
DOI: 10.1016/S1003-6326(16)64213-9

of PCB. However, the fundamental understanding of PCB-ENIG, particularly under adsorbed TEL (ATEL), remains lacking. This situation is mainly attributed to the error in electrochemical measurements that arise from the ohmic drop between the reference electrode (RE) and the working electrode (WE) as well as the uneven current distribution over the WE. Moreover, the Luggin capillary was used to measure the potential of the WE, which may change the thickness and composition of ATEL [5]. Therefore, a new approach to investigate the corrosion failure behavior of PCB-ENIG in situ is necessary. Inspired by previous studies [10−12], a new experimental arrangement was developed in this work to investigate the corrosion of PCB-ENIG under ATEL.

In this work, emphasis was placed on the effect of ATEL on the corrosion behavior of PCB-ENIG. The corrosion behavior of PCB-ENIG under ATEL at different relative humidity (RH) levels (various thickness values) was investigated using a new experimental arrangement and conventional electrochemical techniques, including the measurement of polarization curves, electrochemical impedance spectroscopy (EIS), scanning electron microscopy (SEM), energy-dispersive X-ray spectroscopy (EDS), and X-ray photoelectron spectroscopy (XPS). This research is expected to provide essential insight into the corrosion mechanism of PCB-ENIG under ATEL as well as a basis for optimizing material selection and preventing failures.

2 Experimental

2.1 Materials

The raw material, PCB-ENIG, used in this work was purchased from Sprine Co. (China). The basic parameters of this PCB-ENIG are listed in Table 1. Meanwhile, the schematic diagram of the PCB-ENIG is presented in Fig. 1. As shown in the figure, the PCB-ENIG sample has two identical gold-plated films of 20 mm × 3 mm that were embedded side by side into the upper surface of FR-4. The distance between the two identical gold-plated films, i.e., WE and counter electrode (CE), was 0.5 mm. Two copper wires were welded onto the two electrodes to ensure electrical connection for electrochemical measurements, and the weld points were sealed with silicone. A hole with a diameter of 2 mm was drilled through the PCB-ENIG sample at 0.5 mm apart from the WE and the CE. Before each experiment, the samples were degreased with alcohol for 5 min, rinsed with distilled water for 3 min, and dried in a compressed cold air flow.

Table 1 Basic parameters and treatment of PCB sample

Board material	T_{board}/mm	T_{copper}/μm	$T_{pro\text{-}layer}$/μm
FR-4	0.8	35	0.02

T_{board}—Board thickness; T_{copper}—Copper thickness; $T_{pro\text{-}layer}$—Protective layer thickness

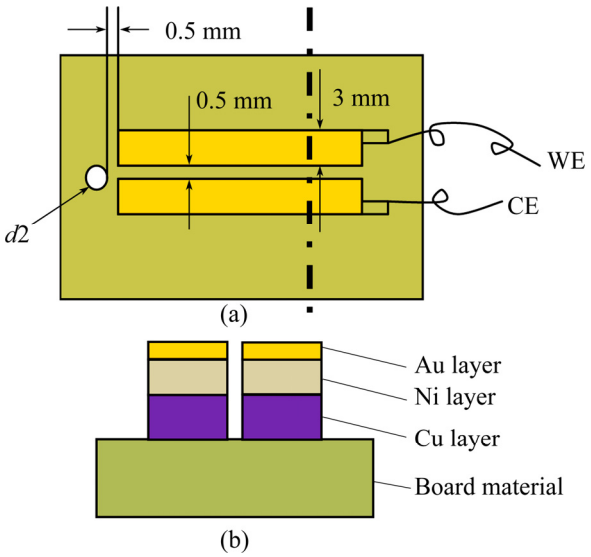

Fig. 1 Schematic diagrams of PCB-ENIG sample: (a) Vertical view; (b) Cross-sectional view

2.2 Design of experimental setup

The TEL that formed in the conventional experimental setup was thicker [8,13]. Consequently, simulating the atmospheric corrosion behavior of the material in a real environment was difficult. To improve the simulation of the corrosion behavior of PCB-ENIG in the marine atmosphere, the setup shown in Fig. 2 was used in the experiment. To achieve certain humidity levels in the reaction chamber, the mixing ratio of dry gas to wet air generated by the humidifier could be adjusted. The solution used in the humidifier was a 3.5% NaCl solution, which was prepared from deionized water and analytical grade reagent NaCl. The U-shaped tube shown in Fig. 2 was filled with saturated NaCl solution. A hole with a diameter of 2 mm was drilled through the cured epoxy resin block. When the experiments were conducted, the PCB-ENIG was fastened to the epoxy resin block and aligned with the hole. Subsequently, a compound mixture of NaCl and agar was embedded into the holes as a salt bridge. The bottom of the epoxy resin block was connected to the U-shaped tube filled with saturated NaCl solution. A saturation calomel electrode (SCE) was set at the U-shaped tube as the RE. This configuration allowed performing electrochemical measurements of the PCB-ENIG electrode under ATEL and minimizing the ohmic drop between RE and WE. Before the experiment, the PCB-ENIG was adjusted in the horizontal direction using a water level.

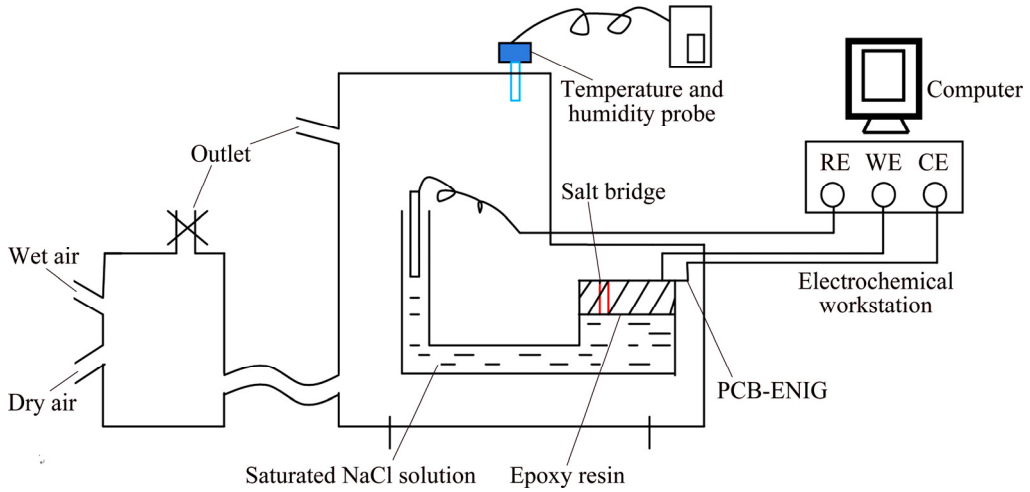

Fig. 2 Schematic diagram of experimental setup

Electrochemical measurements were taken using a potentiostat (Model PARSTAT 2273, Princeton Applied Research, USA). The instrument was controlled with a personal computer and PowerSuite software. The electrochemical cell was a typical three-electrode mode, as shown in Fig. 2. After the system was stabilized for 2 h, cathodic polarization curve measurement was conducted from the open circuit potential (OCP) to −1.6 V (SCE) with a scan rate of 0.5 mV/s.

EIS measurements were performed at OCP with a 10 mV AC perturbation at frequencies ranging from 100 kHz to 10 mHz. The test device and cell configuration for EIS measurements were the same as those for the polarization curve tests. ZSimpWin V3.20 software was used to analyze EIS data with equivalent circuits (ECs). The bulk solution of the electrochemical measurements was a 3.5% NaCl solution. For reproducibility, the cathodic polarization curves and EIS measurements were repeated three times. After the experiment, the specimens under 95% RH were characterized via SEM (Quanta 250, FEI™, USA), EDS (Apollo X, AMETEK®, Inc., USA) and XPS (Thermo ESCALAB 250Xi with an Al K_α X-ray source).

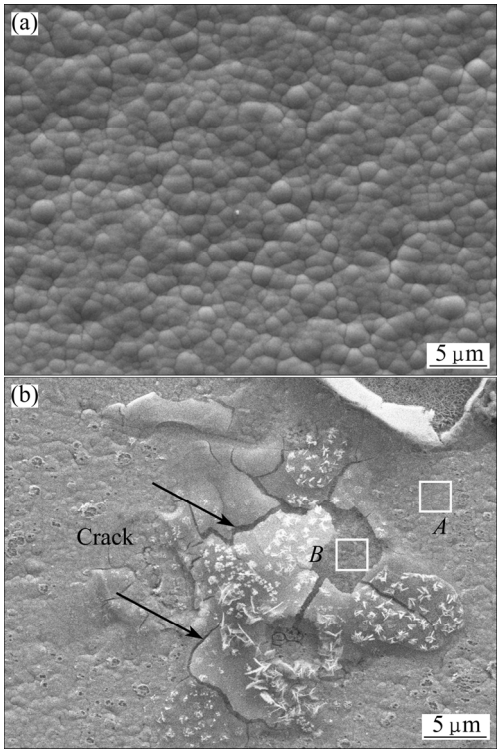

Fig. 3 Surface morphologies of PCB-ENIG under 95% RH before (a) and after 48 h (b) experiment

3 Results and discussion

3.1 SEM analysis

The corrosion morphologies of the PCB-ENIG before and after the Cl-containing thin film experiment were observed with the Everhart–Thornley detector, as shown in Fig. 3. Before the experiment, the sample surface was flat and consisted of similar oval spores. Microporous corrosion occurred on the surface of the PCB-ENIG after 48 h experiment at 95% RH. Several corrosion products were distributed on the surface of the PCB-ENIG; in addition, some microcracks were progressively formed on localized corrosion products, as shown by the arrows in Fig. 3(b). Finally, the expansion of the corrosion products led to the shedding of the surface layer of the protective coating. Table 2 shows the EDS analysis results of the regions in Fig. 3(b). As shown in Table 2, the content of element Cu was higher in region *B*, which indicated that Cu substrate suffered from corrosion. Moreover, a certain amount of Cl was distributed in region *B*, which proved that the product in this region was $Cu_2(OH)_3Cl$ [14]. In actual practice, the electrolyte with Cl^- permeated the inner layer when test time was extended; a galvanic coupling was then formed between the Au layer and the inner layers (Ni and Cu) [9].

Galvanic corrosion also accelerated the corrosion failure of electronic materials.

Table 2 Result of EDS analysis of PCB-ENIG (mole fraction, %)

Region in Fig. 3(b)	O	Cl	Ni	Cu	Au
A	3.77	0.45	82.75	4.57	8.46
B	41.53	6.44	32.19	15.65	4.19

3.2 Measurements of cathodic polarization curves

Although the anodic polarization curve is useful for analyzing the electrochemical corrosion mechanism, some researchers reported that the anodic polarization of TEL is strongly affected by the uneven distribution of current density; moreover, the reproducibility of the anodic polarization curves under TEL is poor [7,15]. Therefore, anodic polarization tests were not performed in the current study. In the case of a cathodic polarization curve, the cathodic current is mainly caused by the reduction of hydrogen and oxygen. The species of the electrochemical reactant diffuse perpendicularly to the electrode surface from the gas phase through ATEL. Charge transfer will occur on the entire electrode surface, and thus, the current will be distributed uniformly on the whole electrode [8,16].

The cathodic polarization curves of the PCB-ENIG after exposure to ATEL with 3.5% NaCl solution at different RH levels and in bulk solution are shown in Fig. 4. The cathodic polarization curves, particularly in bulk solution, could be divided into three regions. Region *A* was the weak polarization region within the vicinity of the OCP; and the cathodic process was the reduction of oxygen, as shown in Eq. (1). With regard to the cathodic polarization curves in the solution, region *B* was the zone for controlling oxygen diffusion. For the cathodic polarization curves under different ATEL thicknesses, the cathodic current density of region *B* was significantly smaller than that in the bulk solution. Moreover, cathodic current density decreased with the thinning of film. The theoretical limited current density (J_{lim}) for 1D diffusion can be calculated according to the Nernst–Fick equation (Eq. (2)). As suggested in Eq. (2), J_{lim} increases with the thinning of the electrolyte layer. However, the results of this experiment, which are presented in Fig. 4, are contrast with this conclusion. Based on the results, the cathodic oxygen reduction process in region *B* under different ATEL thickness values was not controlled by the diffusion of oxygen primarily because the oxygen reduction process was inhibited by low dissolved oxygen concentration under an extremely thin electrolyte film [17]. This phenomenon was previously discovered by WANG and TSURU [18].

$$O_2+2H_2O+4e\rightarrow 4OH^- \quad (1)$$

$$J_{lim}=\frac{nFD_{O_2}[O_2]}{\delta} \quad (2)$$

where n is the number of electrons involved in the oxygen reduction reaction; F is the Faraday constant; D_{O2} and $[O_2]$ are the diffusion coefficient and the concentration of the dissolved oxygen in the TEL, respectively; δ is the thickness of diffusion layer.

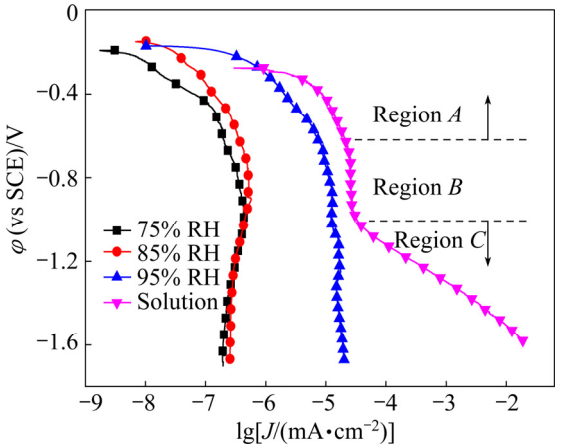

Fig. 4 Cathodic polarization curves for PCB-ENIG under ATEL at different RH levels after 2 h of exposure

A peak perturbed the linear region on the cathodic polarization curves of ATEL with different thicknesses. We deduced that the peaks might be attributed to the reduction of the corrosion product [6,7,19]. To prove this hypothesis, the cathodic polarization curve of the PCB-ENIG under 95% RH was determined by scanning the potential from −1.65 V (vs SCE) to OCP instead of starting from the OCP to the cathodic direction, as shown in Fig. 5. The current density peak in the transition section was clearly not observed during reverse scanning. In addition, the cathodic current density in

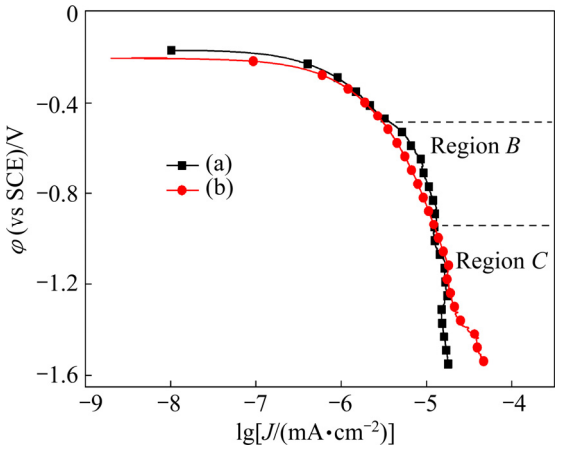

Fig. 5 Cathodic polarization curves of PCB-ENIG under 95% RH after 2 h of exposure: (a) Scanning from OCP to cathodic direction; (b) Scanning from −1.65 V (vs SCE) to OCP

region *B* was significantly less during reverse scanning than that during forward scanning, whereas that in region *C* was greater during reverse scanning. These results were mainly attributed to the reduction of the corrosion products in region *C*; that is, all the corrosion products were reduced. Therefore, based on the aforementioned phenomenon, the cathodic polarization current density in region *B* was larger during forward scanning, whereas that in region *C* was smaller and accompanied by a "small peak".

To further confirm that the peaks were caused by the reduction of the corrosion product, X-ray photoelectron spectroscopy (XPS) was conducted using ESCALAB 250Xi (Thermo Fisher Scientific, USA) with an Al K_α (1486.6 eV) X-ray source. Binding energy was adjusted for charging effect by referencing the C1s peak (284.8 eV). Registered core-level spectra were fitted into the mixed Gaussian–Lorentzian lineshapes according to the Shirley-type background subtraction using Avantage 4.88 software (Thermo Fisher Scientific, USA).

Figure 6 illustrates the comparison between the high-resolution XPS spectra of Cu 2p and Ni 2p. It can be seen in Fig. 6 that, a minimal amount of Cu was found in the corrosion products. The Ni 2p spectra could be divided into three peaks with different binding energies. The first peak was observed at (852.7±0.1) eV and could be associated with the presence of Ni. The second peak was observed at (855.5±0.1) eV, which corresponded to the presence of $Ni(OH)_2$. The last peak was observed at (856.3±0.1) eV, which was associated with the presence of $NiCl_2$ [20,21]. According to Ref. [22],

$$Ni+2OH^- \rightarrow Ni(OH)_2+2e \quad (3)$$

the standard equilibrium potential of reaction (3) is −0.4788 V (vs SCE). In the present work, the reductive potential perturbed by the peaks in the linear region on the cathodic polarization curves was approximately −0.4931 V (vs SCE), which was slightly less than the standard equilibrium potential. We considered that the difference was attributed to the diverse experimental conditions, such as ionic activity and temperature. In summary, the peaks resulted from the reduction process of $Ni(OH)_2$.

In addition, the cathodic current density in the bulk solution in region *C* increased at a faster rate than that under 95% RH. The cathodic current density under 75% RH and 85% RH gradually decreased during the remainder of the experiment. The reduction in H_2O, which was the main reaction in region *C*, was given in Eq. (4). Meanwhile, a strong hydrogen evolution reaction was involved given the adequate moisture in bulk solution, which resulted in the rapid increase of the cathodic current density in this solution. However, the rate of adsorption film formation was less than that of

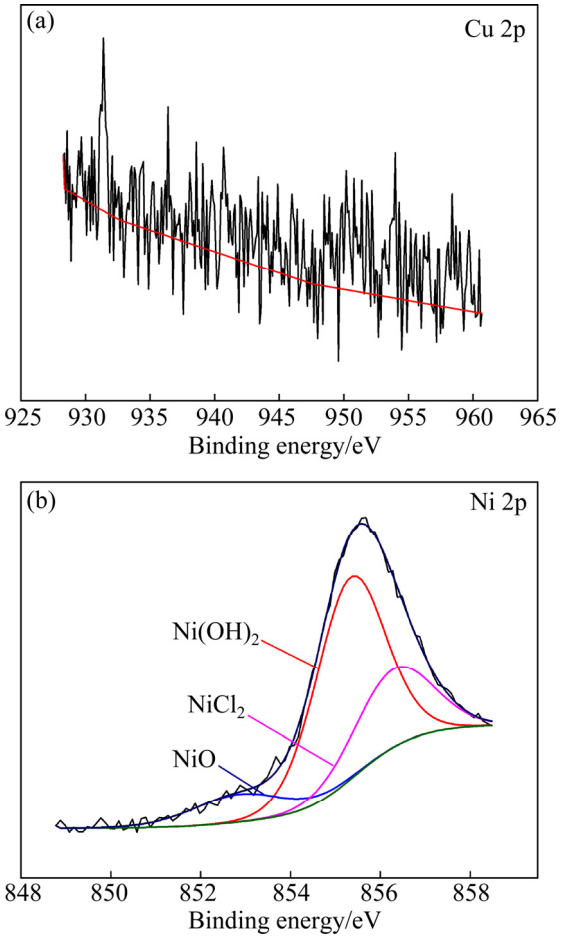

Fig. 6 High-resolution spectra of corrosion products formed on PCB-ENIG: (a) Cu 2p; (b) Ni 2p

hydrogen evolution under 75% RH and 85% RH, which reduced the depolarizing agent (H_2O). Furthermore, ATEL gradually became discontinuous under 75% RH and 85% RH as H evolution progressed, which was contributed to the increase in ion channel resistance and the decrease in cathodic current density [23].

$$2H_2O+2e \rightarrow H_2+2OH^- \quad (4)$$

3.3 EIS measurement

The EIS measurements of the PCB-ENIG under 75% RH and 85% RH were consistent with that under 95% RH. Accordingly, the EIS measurements in bulk solution and under 95% RH were discussed in this study. The EIS and Bode measurements of the PCB-ENIG are presented in Figs. 7 and 8, respectively. As shown in Fig. 7, the Bode plot showed that two time constants were present in bulk solution. Thus, the equivalent electrical circuit shown in Fig. 9(a) was used to fit the EIS measurement of the PCB-ENIG sample to account quantitatively for the corrosion behavior in bulk solution. R_s was the solution resistance, the high-frequency circuit CPE_f–R_f corresponded to the capacitance and the

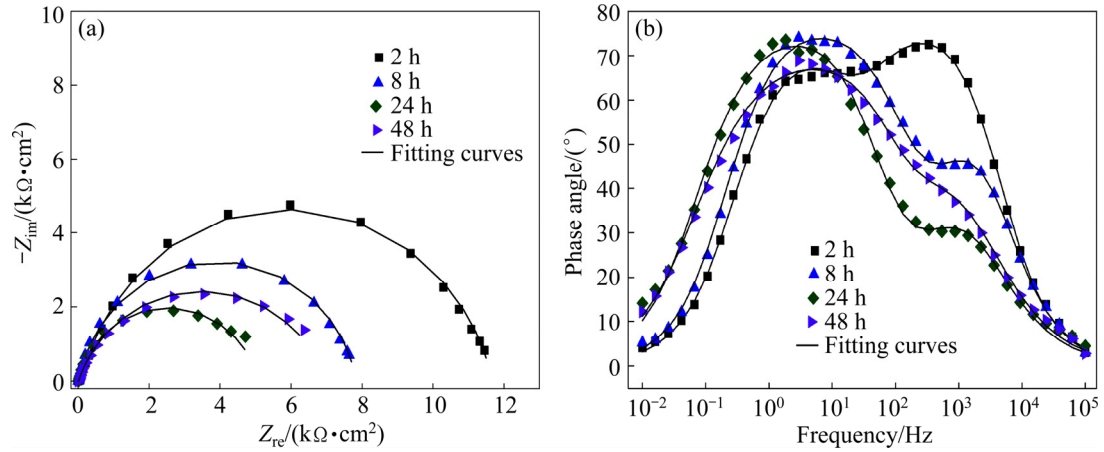

Fig. 7 Nyquist and Bode phase angle plots of PCB-ENIG in 3.5% NaCl bulk solution

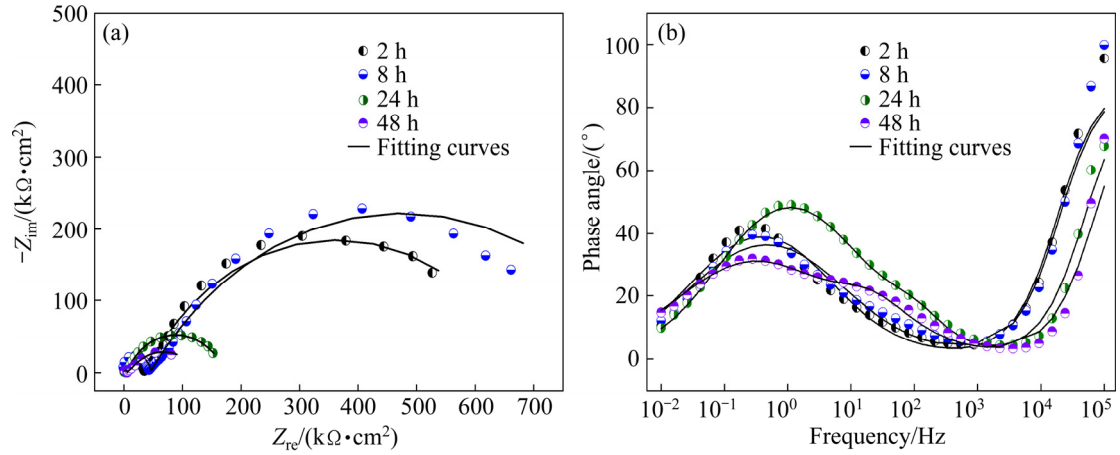

Fig. 8 Nyquist and Bode phase angle plots of PCB-ENIG under 95% RH

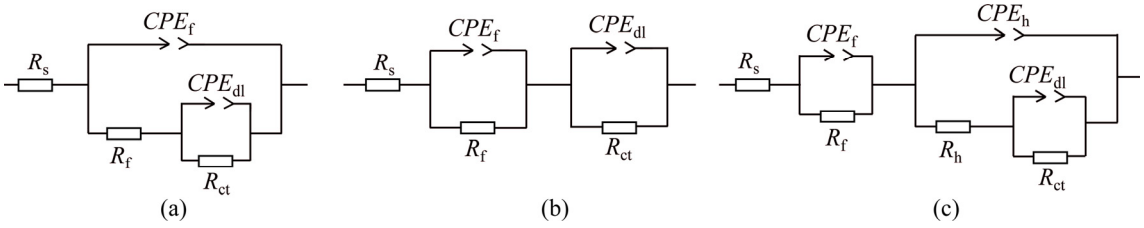

Fig. 9 ECs for PCB-ENIG in bulk solution (a), under ATEL (2 h, 8 h) (b) and under ATEL (24 h, 48 h) (c)

resistance of the corrosion product, and the medium-low frequency circuit CPE_{dl}−R_{ct} corresponded to the double-layer capacitance and the charge transfer resistance.

From the Bode plots shown in Fig. 8, most of the phase angles exceeded 45° when frequency was scanned from high to low. According to NISHIKATA et al [5,24], the model of current distribution could be estimated through EIS. Therefore, the uneven current distribution on the PCB-ENIG electrode in the aforementioned EIS measurements was negligible, and ATEL thickness on the electrode could be uniform and contiguous. In Fig. 8, the Nyquist diagrams for 2 h and 8 h showed two time constants. For the 24 h and 48 h tests, a time constant was observed at high frequency in the EIS measurement, whereas two time constants occurred at medium to low frequencies in the Bode measurement. These findings indicated that the Nyquist plots actually included three time constants for the remainder of the experiment. Consequently, to determine the electrochemical parameters, the EC in Fig. 9(b) was used to fit the EIS measurements into the 2 h and 8 h tests. Figure 9(c) was used to fit the EIS data (for 24 h and 48 h) of the PCB-ENIG under ATEL. R_s was the solution resistance, CPE_f and R_f were related to the corrosion products of the PCB-ENIG, CPE_h and R_h were the constant phase

elements that corresponded to the high-frequency part of the EIS measurements resulting from the microcapillary structure [9,25], CPE_{dl} was a constant phase element that corresponded to the double-layer capacitance, and R_{ct} was the charge transfer resistance. For the constant phase angle element *CPE*,

$$Z_{CPE}=\frac{1}{Y_0(j\omega)^n} \tag{5}$$

where Z_{CPE} is the impedance of the constant phase element, ω is the angular frequency of the AC voltage, and Y_0 and n are the frequency independent parameters. The presence of CPE has been frequently explained by the dispersion effects that can be caused by the microscopic roughness of a surface [8,26].

The fitting results of the EIS measurements of the PCB-ENIG under different conditions are listed in Tables 3−6. The reciprocal of polarization resistance (R_p) is frequently used to represent corrosion rate. In this study, however, the reciprocal of R_{ct} was used to represent the corrosion rate of the PCB-ENIG. R_{ct} is more closely correlated to corrosion rate than R_p when state variables, such as corrosion product, and mass transfer processes affect EIS apart from potential [7,8,27].

Figure 10 shows the time dependence of $1/R_{ct}$ of the PCB-ENIG under ATEL at different RH levels and in bulk solution. As shown in the figure, the corrosion rates of the PCB-ENIG under ATEL increased with increasing RH and were less than that in bulk solution. Overall, corrosion rates increased with exposure time under 85% RH and 95% RH, whereas the change in corrosion rate was minimal under 75% RH. This phenomenon could be explained as follows. In the experiment, dissolved oxygen was deficient under 75% RH because of the

Table 3 Fitting parameters of EIS measurement of PBC-ENIG after exposure to 3.5% NaCl solution

t/h	R_s/(Ω·cm^2)	Corrosion product			Electrical double layer		
		CPE_f/(S·s^n·cm^{-2})	n	R_f/(Ω·cm^2)	CPE_{dl}/(S·s^n·cm^{-2})	n	R_{ct}/(Ω·cm^2)
2	3.681	2.419×10^{-5}	0.9053	579	3.04×10^{-5}	0.821	1.109×10^{4}
8	3.656	3.607×10^{-5}	0.8689	31.3	6.531×10^{-5}	0.8842	7800
24	3.926	1.769×10^{-4}	0.7612	17.22	2.169×10^{-4}	0.9128	5076
48	4.165	1.997×10^{-4}	0.7341	38.52	7.627×10^{-5}	0.8756	6977

Table 4 Fitting parameters of EIS measurement of PCB-ENIG at 75% RH

t/h	R_s/(Ω·cm^2)	Corrosion product			Microcapillary structure			Electrical double layer		
		CPE_0/(S·s^n·cm^{-2})	n	R_0/(Ω·cm^2)	CPE_f/(S·s^n·cm^{-2})	n	R_f/(Ω·cm^2)	CPE_{dl}/(S·s^n·cm^{-2})	n	R_{ct}/(Ω·cm^2)
2	99.22	1.356×10^{-10}	1	1.791×10^{7}				4.883×10^{-10}	0.9432	5.1×10^{8}
8	105.12	1.29×10^{-10}	1	1.102×10^{7}				7.371×10^{-10}	0.8946	3.926×10^{8}
24	126.92	5.036×10^{-10}	0.9969	1.691×10^{6}	1.302×10^{-10}	1	4.261×10^{7}	5.918×10^{-9}	0.5343	2.44×10^{8}
48	131.83	8.695×10^{-11}	1	8.006×10^{7}	8.71×10^{-11}	1	8.08×10^{7}	1.98×10^{-8}	0.5236	1.488×10^{8}

Table 5 Fitting parameters of EIS measurement of PCB-ENIG at 85% RH

t/h	R_s/(Ω·cm^2)	Corrosion product			Microcapillary structure			Electrical double layer		
		CPE_0/(S·s^n·cm^{-2})	n	R_0/(Ω·cm^2)	CPE_f/(S·s^n·cm^{-2})	n	R_f/(Ω·cm^2)	CPE_{dl}/(S·s^n·cm^{-2})	n	R_{ct}/(Ω·cm^2)
2	37.28	3.477×10^{-6}	0.9883	7.854×10^{4}				1.851×10^{-6}	0.6806	1.191×10^{6}
8	42.31	9.046×10^{-10}	0.9065	8.524×10^{4}				1.981×10^{-6}	0.6392	2.046×10^{6}
24	35.56	9.255×10^{-10}	1	3591	7.542×10^{-7}	0.9886	2849	8.651×10^{-6}	0.6932	6.601×10^{5}
48	50.2	3.653×10^{-10}	1	1.778×10^{4}	4.79×10^{-6}	0.5656	1.302×10^{5}	1.235×10^{-4}	0.9298	1.553×10^{5}

Table 6 Fitting parameters of EIS measurement of PCB-ENIG at 95% RH

t/h	R_s/(Ω·cm^2)	Corrosion product			Microcapillary structure			Electrical double layer		
		CPE_{hf}/(S·s^n·cm^{-2})	n	R_{hf}/(Ω·cm^2)	CPE_f/(S·s^n·cm^{-2})	n	R_f/(Ω·cm^2)	CPE_{dl}/(S·s^n·cm^{-2})	n	R_{ct}/(Ω·cm^2)
2	21.51	2.467×10^{-10}	1	3.616×10^{4}				3.74×10^{-6}	0.6549	6.53×10^{5}
8	29.76	1.829×10^{-10}	1	4.483×10^{4}				2.701×10^{-6}	0.6074	8.6×10^{5}
24	26.92	9.255×10^{-10}	1	3591	7.542×10^{-7}	0.9886	2849	8.651×10^{-6}	0.6932	1.666×10^{5}
48	31.83	6.49×10^{-6}	0.8395	3839	4.224×10^{-10}	0.998	5654	2.185×10^{-5}	0.5765	1.312×10^{5}

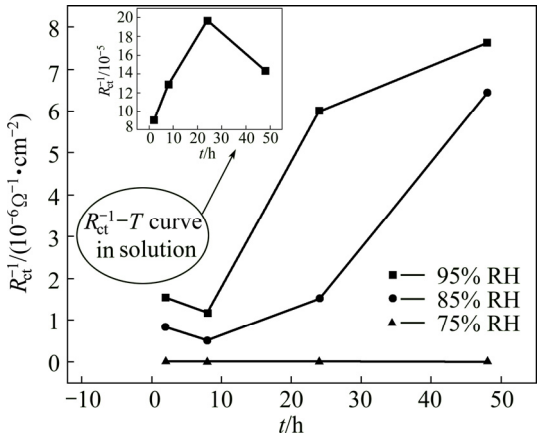

Fig. 10 Time dependence of $1/R_{ct}$ under different RH levels and in bulk solution

extremely thin electrolyte layer. In addition, a small amount of the corrosion products also hindered the corrosion process. Thus, the corrosion rate of the PCB-ENIG under 75% RH was always smaller. Permeating into the micropores on the surface of the PCB-ENIG was easy for Cl^- when the thickness of the electrolyte film increased as a result of increasing humidity. This condition caused the corrosion of the Ni layer of the PCB-ENIG. Nevertheless, the corrosion products that accumulated in the micropores inhibited the corrosion process and decreased corrosion rate. However, as immersion time progressed, some microcracks were gradually produced on the local corrosion area. These cracks expanded progressively and finally led to Cl^- progressively infiltrating into the substrate Cu and causing Cu corrosion. Moreover, galvanic coupling was formed between the Au layer and the lower electrode potential inner layers (Ni and Cu) during the later stage when the electrolyte permeated across the outer layer. This condition accelerated the corrosion of the substrate of the PCB-ENIG. Thus, corrosion rate increased at the end of the experiment. The aforementioned phenomenon is consistent with the SEM image of the PCB-ENIG.

Furthermore, Fig. 10 clearly shows that the increment of the corrosion rate of the PCB-ENIG under 95% RH is less than that under 85% RH after 24 h. This phenomenon could be explained as follows. During the initial stage, the corrosion rate of the PCB-ENIG at 95% RH was higher than that at 85% RH. However, after a long time exposure, more corrosion products were formed on the WE surface at 95% RH than those at 85% RH; thus, anodic dissolution, to some extent, was inhibited by the corrosion product at 95% RH, which resulted in the lower increment of corrosion rate. This result showed that the corrosion process was controlled by the anodic process during the later period of the test.

4 Conclusions

1) Micropore corrosion mainly occurred in the PCB-ENIG under ATEL. During the initial stage of the experiment, the corrosion process was inhibited by the corrosion products that accumulated in the micropores of the PCB-ENIG. However, after a long time exposure, the process gradually produced microcracks in the local corrosion area, which expanded progressively and finally led to Cl^- gradually infiltrating into the substrate Cu and causing Cu corrosion. Thus, corrosion rate increased at the end of the experiment.

2) The cathodic process of the PCB-ENIG under a thin film environment was dominated by the reduction of dissolved oxygen, corrosion products, and H_2O. The cathodic current density of the PCB-ENIG increased progressively with increasing RH. Moreover, its cathodic current density in the solution was greater than that under a thin electrolyte film.

3) When the polarization potentials were located in a more negative region, the cathodic polarization current density gradually decreased under 75% RH and 85% RH. This phenomenon was mainly attributed to the depolarization rate of H_2O being greater than the formation rate of the adsorption film to a certain extent, which decreased net water content or ATEL thickness. It also inhibited the diffusion process of metal cations to a considerable extent. The anodic process subsequently became a controlled step in the extremely thin liquid film during the remainder of the experiment.

References

[1] DING Kang-kang, LI Xiao-gang, XIAO Kui, DONG Chao-fang, ZHANG Kai, ZHAO Rui-tao. Electrochemical migration behavior and mechanism of PCB-ImAg and PCB-HASL under adsorbed thin liquid films [J]. Transactions of Nonferrous Metals Society of China, 2015, 25(7): 2446−2457.

[2] LEYGRAF C, GRAEDEL T. Atmospheric corrosion [M]. New York: John Wiley & Sons, 2000: 142−196.

[3] ZOU Shi-wen, LI Xiao-gang, DONG Chao-fang, LI Hui-yan, XIAO Kui. Effect of mold on corrosion behavior of printed circuit board-copper and ENIG finished [J]. Acta Metall Sin, 2012, 48: 687−695. (in Chinese)

[4] AMBAT R, MøLLER P. Corrosion investigation of material combinations in a mobile phone dome–key pad system [J]. Corros Sci, 2007, 49: 2866−2879.

[5] MAHDY G A, NISHIKATA A, TSURU T. AC impedance study on corrosion of 55%Al−Zn alloy-coated steel under thin electrolyte layers [J]. Corros Sci, 2000, 42: 1509−1521.

[6] ZHONG X K, ZHANG G A, QIU Y B, CHEN Z Y, GUO X P, FU C Y. The corrosion of tin under thin electrolyte layers containing chloride [J]. Corros Sci, 2013, 66: 14−25.

[7] HUANG H L, GUO X P, ZHANG G A, DONG Z H. The effects of temperature and electric field on atmospheric corrosion behaviour of PCB-Cu under absorbed thin electrolyte layer [J]. Corros Sci, 2011, 53: 1700−1707.

[8] CHENG Y L, ZHANG Z, CAO F H, LI J F, ZHANG J Q, WANG J M, CAO C N. A study of the corrosion of aluminum alloy 2024-T3 under thin electrolyte layers [J]. Corros Sci, 2004, 46: 1649−1667.
[9] ZOU S W, LI X G, DONG C F, DING K K, XIAO K. Electrochemical migration, whisker formation, and corrosion behavior of printed circuit board under wet H_2S environment [J]. Electrochim Acta, 2013, 114: 363−371.
[10] LIU W J, CAO F H, JIA B L, ZHENG L Y, ZHANG J Q, CAO C N, LI X G. Corrosion behaviour of AM60 magnesium alloys containing Ce or La under thin electrolyte layers. Part 2: Corrosion product and characterization [J]. Corros Sci, 2010, 52: 639−650.
[11] CRUZ R P V, NISHIKATA A, TSURU T. Pitting corrosion mechanism of stainless steels under wet-dry exposure in chloride-containing environments [J]. Corros Sci, 1998, 40: 125−139.
[12] HUANG Hua-liang, PAN Zhi-quan, GUO Xing-peng, QIU Yu-bing. Effects of direct current electric field on corrosion behaviour of copper, Cl^- ion migration behaviour and dendrites growth under thin electrolyte layer [J]. Transactions of Nonferrous Metals Society of China, 2014, 24(1): 285−291.
[13] ZHOU He-rong, LI Xiao-gang, DONG Chao-fang, XIAO Kui, FENG Hao. Corrosion of aluminum alloy 7A04 under thin electrolyte layers [J]. J Beijing Univ Sci Technol, 2008, 30: 880−887. (in Chinese)
[14] MA A L, JIANG S L, ZHENG Y G, KE W. Corrosion product film formed on the 90/10 copper–nickel tube in natural seawater: Composition/structure and formation mechanism [J]. Corros Sci, 2015, 91: 245−261.
[15] ZHANG T, CHEN C M, SHAO Y W, MENG G Z, WANG F H, LI X G, DONG C F. Corrosion of pure magnesium under thin electrolyte layers [J]. Electrochim Acta, 2008, 53: 7921−7931.
[16] SHI Yan-yan. The electrochemical studies of atmospheric corrosion of typical metals [D]. Zhejiang: Zhejiang University, 2008: 29−56. (in Chinese)
[17] JIANG Jing. The role of liquid dispersion in gas/liquid/solid multiphase corrosion systems [D]. Qingdao: Ocean University of China, 2009: 3−9. (in Chinese)
[18] WANG J, TSURU T. An investigation on oxygen reduction under thin electrolyte layer using Kelvin probe reference electrode [J]. Journal of Chinese Society for Corrosion and Protection, 1995, 15: 180−188. (in Chinese)
[19] LIAO Xiao-ning, CAO Fa-he, CHEN An-na, LIU Wen-juan, ZHANG Jian-qing, CAO Chu-nan. In-situ investigation of atmospheric corrosion behavior of bronze under thin electrolyte layers using electrochemical technique [J]. Transactions of Nonferrous Metals Society of China, 2012, 22(5): 1239−1249.
[20] MARCUS P, GRIMAL J M. The anodic dissolution and passivation of Ni single bond Cr single bond Fe alloys studied by ESCA [J]. Corros Sci, 1992, 5: 805−814.
[21] MCINTYRE N S, COOK M G. X-ray photoelectron studies on some oxides and hydroxides of cobalt, nickel, and copper [J]. Anal Chem, 1975, 47: 2208−2213.
[22] CAO Chu-nan. Principles of electrochemistry of corrosion [M]. Beijing: Chemical Industry Press, 2008. (in Chinese)
[23] LIU Z J, WANG W, WANG J, PENG X, WANG Y H, ZHANG P H, WANG H J, GAO C J. Study of corrosion behavior of carbon steel under seawater film using the wire beam electrode method [J]. Corros Sci, 2014, 80: 523−527.
[24] NISHIKATA A, ICHIHARA Y, TSURU T. An application of electrochemical impedance spectroscopy to atmospheric corrosion study [J]. Corros Sci, 1995, 37: 897−911.
[25] NOTTER I M, GABE D R. Porosity of electrodeposited coatings: Its cause, nature, effect and management [J]. Corros Rev, 1992, 10: 217−280.
[26] CHAVARIN J U. Electrochemical investigations of the activation mechanism of aluminum [J]. Corrosion, 1991, 47: 472−479.
[27] LIAO X N, CAO F H, ZHENG L Y, LIU W J, CHEN A A, ZHANG J Q, CAO C N. Corrosion behaviour of copper under chloride-containing thin electrolyte layer [J]. Corros Sci, 2011, 53: 3289−3298.

原位研究 PCB-ENIG 在吸附薄液膜下的大气腐蚀行为

易 盼[1]，肖 葵[1]，丁康康[1,2]，李 刚[1]，董超芳[1]，李晓刚[1,3]

1. 北京科技大学 腐蚀与防护中心，北京 100083；
2. 中国船舶重工集团公司 第七二五研究所 海洋腐蚀与防护国家重点实验室，青岛 266101；
3. 中国科学院 宁波材料技术与工程研究所，宁波 315201

摘 要：通过阴极极化曲线、交流阻抗谱以及 SEM、XPS，原位研究了相对湿度对无电镀镍金印制电路板(PCB-ENIG)在吸附薄液膜下的影响机制。结果表明：PCB-ENIG 板在薄液膜下的阴极过程主要包括 O_2、腐蚀产物和 H_2O 的还原过程。阴极电流密度随相对湿度的增加而增加，并且均小于溶液中阴极电流密度，表明扩散过程并不是阴极氧化还原过程的控制步骤。极化电位较负时，75%和 85%相对湿度下的阴极极化电流密度逐渐减小。随着腐蚀产物的增加，试验后期腐蚀过程由阳极过程控制。

关键词：电子材料；吸附薄液膜；阴极极化曲线；电化学交流阻抗谱；相对湿度

(Edited by Xiang-qun LI)